Experimental and image-inversion optimization aspects of thermal-wave diffraction tomographic microscopy

Lena Nicolaides and Andreas Mandelis
Photothermal and Optoelectronic Diagnostics Laboratories, Department of Mechanical and Industrial Engineering, University of Toronto, Toronto M5S 3G8, Canada

Abstract: Thermal-wave Slice Diffraction Tomography (TSDT) is a photothermal imaging technique for non-destructive detection of sub-surface cross-sectional defects in opaque solids in the very-near-surface region (μm-mm). Conventional reconstructions of the well-posed propagating wave-field tomographies cannot be applied to the ill-posed thermal wave problem. Photothermal tomographic microscopy is used to collect experimental data that are numerically inverted with the Tikhonov regularization method to produce thermal diffusivity cross-sectional images in materials. Multiplicity of solutions, which is inherent to ill-posed problems, is resolved by adopting the L-curve method for optimization. For tomographic imaging of sub-surface defects, a new high-resolution radiometric setup is constructed, which reduces the broadening of images associated with previous low-resolution setups.

OCIS codes: (290.3200) Inverse scattering; (100.6950) Tomographic image processing

---

References and Links

1. G. Busse and K.F. Rank, "Stereoscopic Depth Analysis by Thermal Wave Transmission for Non-Destructive Evaluation," Appl. Phys. Let. **42**, 366 (1983).
2. A. Mandelis, "Theory of Photothermal Wave Diffraction Tomography via Spatial Laplace Spectral Decomposition," J. Phys. A: Math. General **24**, 2485 (1991).
3. A. Mandelis, "Theory of Photothermal Wave Diffraction and Interference in Condensed Phases," J. Opt. Soc. Am. A **6**, 298 (1989).
4. M. Munidasa and A. Mandelis, "Photopyroelectric Thermal-Wave Tomography of Aluminum with Ray-Optic Reconstruction," J. Opt. Soc. Am. A **8**,1851 (1991).
5. O. Pade and A. Mandelis, "Computational Thermal-Wave Slice Tomography with Backpropagation and Transmission Reconstructions," Rev. Sci. Instrum. **64**, 3548 (1993).
6. A. Mandelis, "Green's Functions in Thermal Wave Physics: Cartesian Coordinate Representations," J. Appl. Phys., **78** (2), 647 (1995).
7. L. Nicolaides and A. Mandelis, "Image-Enhanced Thermal-Wave Slice Diffraction Tomography with Numerically Simulated Reconstructions," Inv. Prob. **13**, 1393 (1997).
8. L. Nicolaides, M. Munidasa and A. Mandelis, "Thermal-Wave Infrared Radiometric Slice Diffraction Tomography with Back-Scattering and Transmission Reconstructions: Experimental," Inv. Prob. **13**, 1413 (1997).
9. A. Mandelis, *Diffusion Wave Fields: Green Functions and Mathematical Methods* (Springer, New York, in press).
10. A.N. Tikhonov, "On Stability Of Inverse Problems," Dokl. Acad. Nauuk USSR, **39**(5), 195 (1943).
11. B. Hofmann, *Regularization for Applied and Ill-Posed Problems,* (Teubner, 1986).
12. C. Hansen, "Analysis of Disrete Ill-Posed Problems by Means of the L-Curve," SIAM Review, **34**, 561 (1992).
13. C. Hansen and D. P. O'Leary, "The use of the L-curve in the regularization of discrete ill-posed problems," SIAM J. Sci. Comput. **14**, 1487 (1993).
14. A. Mandelis and M. Mieszkowski, "Thermal Wave Sub-Surface Defect Imaging and Tomography Apparatus," U.S. Patent Number 4, 950, 897; Date: August 21, 1990.
15. L. Qian and P. Li, "Photothermal radiometry measurement of thermal diffusivity," Appl. Opt. **29**, 4241 (1990).

Received October 27, 2000; Revised December 15, 2000

16. G. Busse, D. Wu and W. Karpen, “Thermal Wave Imaging with Phase Sensitive Modulated Thermography,” J. Appl. Phys. **71**, 3962 (1992).
17. A.C. Kak and M. Slaney, *Principles of Computerized Tomographic Imaging,* (IEEE Press, New York, 1988).
18. A. Mandelis, “Diffusion waves and their uses,” Physics Today, **29**, August 2000.
19. E. Miller, L. Nicolaides and A. Mandelis, “Nonlinear Inverse Scattering Methods for Thermal-Wave Slice Tomography: A Wavelet Domain Approach,” J. Opt. Soc. Am. A, **15**, 1545 (1998).

---

1. Introduction

Thermal-wave inverse problems are ill-posed problems, meaning they either have no solution, no unique solution or unstable solution. The main difficulty with such problems is that a regularization method is needed to isolate a unique solution. The ill-posed problem examined in this work is associated with Thermal-wave Slice Diffraction Tomography (TSDT), a relatively new cross-sectional photothermal imaging method for the detection of sub-surface defects in materials through mapping of the cross-sectional slice thermal diffusivity. Images obtained from conventional thermal wave imaging are two dimensional "projections" of sub-surface features in the sense that the image is formed by mapping the sample surface temperature in a two dimensional raster scan without regard to the actual depth position of scatterers. Cross-sectional photothermal tomographic imaging refers to a line scan that obtains information about a sample cross-section normal to its surface plane. Although some early work has been done in obtaining elementary depth information on sub-surface features (defects) [1], it was not until the 1990s that TSDT was introduced in this Laboratory in a concerted effort to develop a viable tomographic imaging technology using thermal waves [2-8]. Multiplicity of solutions was found to be an inherent feature to the (ill-posed) thermal-wave tomographic reconstruction problem. As a result, a “brute-force” approach [7,8] was used to obtain a proper (reasonably stable) solution. However, in order to pinpoint a reasonable solution, it is important to adapt a rigorous optimization approach. This is especially important, if TSDT is to be successfully implemented for practical and industrial applications. In this work, a suitable optimization algorithm in TSDT is developed in conjunction with a high-resolution photothermal radiometric experimental tomographic setup. The purpose of such a high-resolution setup is to overcome the problem of image broadening associated with earlier low-resolution experimental set-ups [8]. The optimization algorithm is necessary for speeding up the image reconstruction procedure under optimal sensitivity and noise conditions.

2. Theoretical and Numerical Model

A forward theory of the thermal wave propagation process has been developed utilizing thermal wave diffraction as an integral solution of the pseudo-wave Helmholtz equation [2,3]. The theoretical model that represents the behavior of a three dimensional thermal wave [6,9] is correlated with the Born approximation utilizing the Tikhonov regularization method to invert almost singular matrices resulting from the ill-posedness of the inverse thermal-wave problem [7]. The Born approximation results in the following integral equation [7]

$$T_S(\mathbf{r}) = \iiint_{V_0} G_0(\mathbf{r}-\mathbf{r}_0) T_i(\mathbf{r}_0) F(\mathbf{r}_0) dV_0 \qquad (1)$$

where $\mathbf{r}$ and $\mathbf{r}_0$ are the coordinates of the observation point and the source point, with respect to the origin, T_s is the scattering field, G_0 is the appropriate Green function. $F(\mathbf{r})$ is the object function and it represents the inhomogeneities of scattering object region R. The object function $F(\mathbf{r})$ is zero at every point outside region R and has a non-zero value that represents the ratio of thermal diffusivities inside region R. If the inhomogeneous region R is removed

#26871 - $15.00 US
Received October 27, 2000; Revised December 15, 2000

from boundary S, then $F(\mathbf{r})$ would be zero everywhere and thus the medium inside the volume enclosed by the boundary S would be totally homogeneous. Therefore, $F(\mathbf{r})$ is defined as follows:

$$F(\mathbf{r}) = \begin{cases} q_0^2[n^2(\mathbf{r})-1]; & \mathbf{r} \in R \\ 0; & \mathbf{r} \notin R \end{cases} \tag{2a}$$

with

$$n(\mathbf{r}) = \sqrt{\frac{\alpha_0}{\alpha(\mathbf{r})}} \tag{2b}$$

and

$$q_0 = (1+i)\left(\frac{\omega}{2\alpha_0}\right)^{1/2} \tag{2c}$$

where q_0 is the complex wavenumber and $n(\mathbf{r})$ is a measure of the variation of the thermal diffusivity values in the scattering object R from that of the surrounding (reference) region R_0. The ratio in equation (2b) has been symbolized by $n(\mathbf{r})$ deliberately, to suggest the analogy of this parameter to the effects of variations in the refractive index in conventional optical propagating fields [2,3]. The object function reconstructed is the non-dimensional function $n^2(\mathbf{r})$-1, referred to as the *contrast* of the image. The background thermal diffusivity, α, thermal conductivity, k, modulation frequency, f, and laser beam size, w, are the necessary input parameters for calculating the homogeneous thermal-wave field.

Equation (1) is defined by a system of linear equation as $\mathbf{Ax}=\mathbf{b}$, where $\mathbf{A}$ is an ill-conditioned matrix that represents the discretized version of the intergral equation (1), $\mathbf{b}$ is the experimental known vector and $\mathbf{x}$ is a sought solution. To solve the ill-posed problem, Tikhonov's regularization method is used and the regularized solution, $\mathbf{x}_\sigma$, as proposed by Tikhonov is [10],

$$\mathbf{x}_\sigma = \min\{\|\mathbf{Ax}-\mathbf{b}\|_2 + \sigma\|\mathbf{L}(\mathbf{x}-\mathbf{x}_0)\|_2\} \tag{3}$$

where $\mathbf{x}_0$ is an initial estimate of the solution, and matrix $\mathbf{L}$ is either the identity matrix $\mathbf{I}$ or a discrete approximation to a derivative operator. The regularization parameter, σ, controls the weight given to minimization of the side constraint, $\|\mathbf{L}(\mathbf{x}-\mathbf{x}_0)\|_2$, relative to minimization of the residual norm, $\|\mathbf{Ax}-\mathbf{b}\|_2$. For this work, no particular knowledge about the desired solution is available, so $\mathbf{x}_0=\mathbf{0}$ is used; also matrix $\mathbf{L}$ is set as the identity matrix, $\mathbf{I}$. In an ill-posed problem, small perturbations in the experimental data cause large perturbations in the solution [11]. Therefore, a regularization method must be implemented to stabilize the problem. The fundamental idea of Tikhonov regularization is to introduce a trade-off between the size of the residual norm $\|\mathbf{Ax}_\sigma-\mathbf{b}\|_2$ and the side constraint $\|\mathbf{x}_\sigma\|_2$. By choosing a suitable regularization parameter, σ, a satisfactory solution can be found for which the two constraints are balanced [12]. Too much regularization leaves out information actually available in $\mathbf{b}$ while too little regularization produces a solution dominated by errors. One method for choosing the optimal regularization parameter is the L-curve method [12,13]. This is an *a posteriori* method based on plotting the side constraint of the solution versus the residual norm for a particular regularization parameter. A schematic of the L-curve is shown in Figure

Received October 27, 2000; Revised December 15, 2000

1 and, as can be seen, the name “L-curve” is derived from the fact that the curve is L-shaped. The “corner” of the curve corresponds to a regularization parameter that is optimal [12]. The “flat” part of the L-curve is dominated by regularization errors occurring from oversmoothing and the “vertical” part is dominated by perturbation errors occurring from undersmoothing. Thus the corner of the L-curve corresponds to a solution in which there is a fair balance between the regularization and perturbation errors.

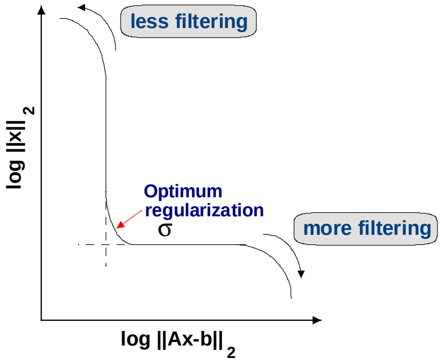

Fig. 1. L-curve method: the corner of the curve corresponds to optimum regularization.

3. Experimental Method

The experimental technique needed to acquire the scanned data for thermal-wave tomograms is described briefly. The data are obtained at one cross-section from different laser and detector positions. Historically, the first detection method used to obtain tomographic slice data was photopyroelectric detection [4,14], which was limited to transmission measurements. A photothermal infrared radiometric detection method then followed. However, a disadvantage was that a low-spatial-resolution setup was used, which resulted in image broadening [8]. In the low-spatial-resolution set-up the beam spot size was focused to about 50μm and the dimensions of the detector active area were 50μm x 50μm. The major disadvantage of the system was that the collected infrared radiation with paraboloidal mirrors, was focused to a spot size much larger (~70μm) than the detector active area. This not only led to a significant loss of signal but also made the detector size the limiting factor of the observed image area. When a detector with an active area of 1mm x 1mm was used [8], there was no signal loss, but a broader image was seen. This broadening, due to the detection size, was improved by constructing a new high-resolution experimental configuration for photothermal radiometric tomographic application. In the new set-up the infrared radiation is collected by two diffraction-limited reflecting objectives as oppose to the paraboloidal mirrors. Figure 2 illustrates the experimental configuration. A 514.5-nm cw Innova Ar^+ laser from Coherent is modulated and then focused onto a sample to a spot size of approximately 27 μm. The modulation is performed by an external acousto-optic modulator (AOM) (ISOMET 1201E-1). The blackbody radiation from the optically excited sample is collected and collimated by the two axially aligned reflecting objectives. It is then focused onto a liquid-nitrogen-cooled photoconductive HgCdTe (Mercury-Cadmium-Telluride) detector (EG&G Judson Model J15D12-M204-S050U). The HgCdTe detector has an active square size of 50 μm x 50 μm and a bandwidth of 2-12μm. The detector is operated at a cryogenic temperature of 77 K since its efficiency increases with decreasing temperature. An antireflection-coated germanium window with a transmission bandwidth of 2-14 μm is mounted in front of the detector to block any visible radiation from the pump laser. Before being sent to the digital lock-in amplifier (Stanford Research System Model SR850), the

#26871 - $15.00 US
Received October 27, 2000; Revised December 15, 2000

photothermal-radiometric signal is amplified by a preamplifier (EG&G Judson Model PA-300) specifically designed for operation with the HgCdTe detector. The lock-in amplifier, which is interfaced with a personal computer, receives the preamplifier output and rejects all stray signals except those that have the same modulation frequency as the excitation beam. This process of data acquisition, storage, and scanning is fully automated. The instrumentation has the ability to perform in either reflection or transmission mode by directing the laser beam to the front or rear surface of the sample using removable mirrors.

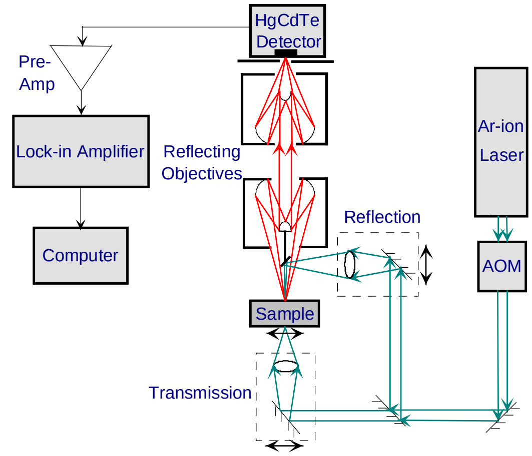

Fig. 2. High-resolution tomographic radiometric microscope experimental set-up.

In the experimental set-up, both the modulated heating source and the detector are localized, and therefore can be scanned independently. For each laser position, data are collected at several detector positions along a straight line. This defines the cross-sectional plane (tomographic scan) to be imaged, e.g. line PQ in Figure 3. The scan for the same cross-section is repeated for different laser positions. The experimental information is then used to reconstruct the respective cross sectional slice, using the method outlined in section 2. In practice, moving the sample becomes equivalent to moving the detector. For example, the transmission tomographic scan is performed by first positioning the laser and then moving the sample and laser together over the detector. Figure 4 illustrates a tomographic scan in transmission with three detection points and three laser positions, which ensures that the same cross-section is maintained at all times. When detector and laser are aligned with each other the signal is highest. For laser position #1, the maximum occurs at point 3; for laser position #2, the maximum occurs at point 2; and for laser position #3, the maximum occurs at point 1. These three scans (or more) can be used to reconstruct the experimental tomographic scan. In reflection mode the tomographic scan is achieved by attaching a 45° mirror to the first reflective objective, Fig. 2. The dead optical field that the reflective objective produces limits the size of the mirror. For this reason the dimensions of the mirror are 3 mm×2 mm, limiting the tomographic scan to 1.5 mm (3 mm/2). Experimentally, this limit was found to be 0.7 mm and thus tomographically only a maximum cross-section of 0.7 mm can be investigated at a time with the current set-up.

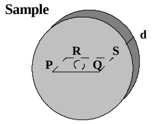

Fig. 3. Line scan for cross-sectional imaging, of sample thickness *d* with a round subsurface defect.

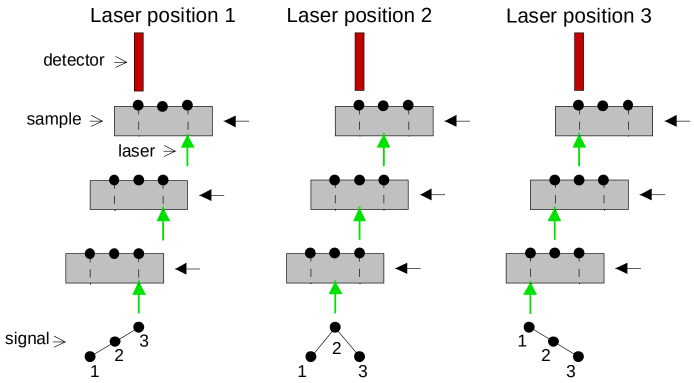

Fig. 4. Schematic of experimental method of thermal-wave tomographic scans for 3 laser and 3 detection positions.

4. Tomographic Experiments

Steel is a good thermal emitter and can be reasonably assumed homogeneous for testing the tomographic method. Two samples of a mild steel alloy with subsurface defects were used for the tomographic experiments. Sample 1 contained a subsurface hole of diameter 0.6 mm located 0.1 mm below the surface and had a thickness of 2 mm. The thermal diffusivity of the sample was measured in transmission and was found to be α=1.1x10^{-5}m^2/s, in agreement with literature reports [15]. Since the experimental setup in reflection was limited by the tomographic range, a second steel sample (similar geometry as Sample 1) was customized to investigate the reflection experiments. Sample 2 had two 0.3-mm diameter defects, 0.1 mm and 0.2 mm deep in the material, respectively. The thermal diffusivity of this steel material was measured in transmission and was found to be α=1.55x10^{-5}m^2/s.

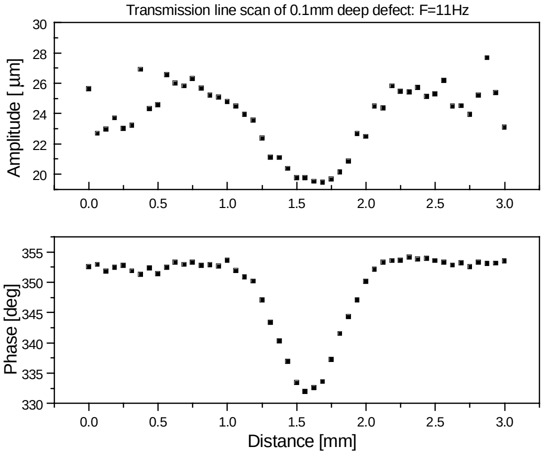

Fig. 5. Amplitude and phase in transmission of the line scan, *f=11* Hz.

Received October 27, 2000; Revised December 15, 2000

First, Sample 1 was tested in transmission at a modulation frequency, $f=11$ Hz with a thermal diffusion length, $\mu=(\alpha/\pi f)^{1/2}=0.56$ mm. The tomographic scan was taken along a constant cross section. The defect imaged lay 0.1 mm from the front surface and was 0.6 mm in diameter. Figure 5 shows a conventional line scan along the imaged line. A line scan is achieved by scanning the laser and the detector together. This provides information about the defect's x-location. Both the amplitude and phase of the scan exhibit a minimum at the defect location. This behavior is due to the fact that the defect (air) is a poor thermal conductor and thus acts as a thermal impedance to heat propagation in transmission. In general, the amplitude of the signal is influenced by surface blemishes and reflectance, whereas the phase is largely unaffected and truly represents subsurface defects [16]. From the line scan data the defect is found to be at the center of the scan (x=1.5 mm). Figure 6 represents amplitude and phase images of the transmission tomographic scan with five laser positions along the cross-section (3 mm) at 49 detector points. The five laser positions used were x_f = 0.5, 1, 1.5, 2, 2.5 mm. From the tomographic scan, the information given from a line scan can also be obtained: In the former scan, the maximum signal always occurs when the laser and detector are aligned with each other. Therefore, the locus of maxima at all laser positions can produce the line scan. This is the diagonal line (x=y) in the experimental data as seen in Figure 6, where a minimum is observed for both amplitude and phase. These are equivalent to the line scan of Fig. 5.

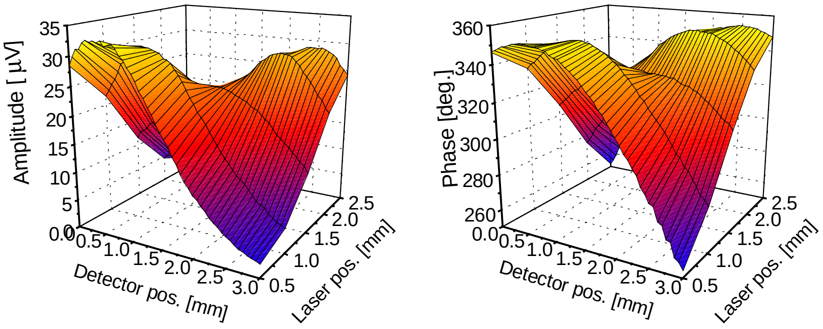

Fig. 6. Transmission tomographic spatial-frequency scan of 0.1-mm deep defect at $f=11$ Hz. Amplitude and phase.

The homogeneous field of the samples, i.e the background field with no defect, was also investigated for both transmission and reflection modes. Figure 7 shows the field in reflection for f=80 Hz. The response is shown on a two-dimensional graph. Each laser position corresponds to a maximum in the experimental data. The theoretical fields, equations (20a) and (20b) in Ref [7] for reflection and transmission, respectively, are also shown at each laser position for f=80 Hz. The agreement between theory and experiment at all frequencies and experimental modes is excellent although there is a slight instrumental asymmetry on the right-hand side of the experimental data.

Reflection tomographic scans at modulation frequencies of 80 Hz and 300 Hz were performed subsequently for two defects, 0.1-mm and 0.2-mm deep. The x-location of the defects was always at the center of the scan. The tomographic scans in reflection at 80 Hz were performed for 11 laser positions, x_f = 0, 0.05, 0.1, 0.15, 0.2, 0.25, 0.3, 0.35, 0.4, 0.45, 0.5 mm, and 21 detector positions. The length of this scan was 0.5 mm and the thermal diffusion length at 80 Hz was 0.25 mm. The 0.1-mm deep defect was centered at (x_c=0.15 mm, y_c=0.25 mm). The 0.2-mm deep defect was centered at (x_c=1.5 mm, y_c=0.35 mm). Similar tomographic experiments were performed at the same locations using 300 Hz. The thermal diffusion length at this frequency was 0.13 mm. The length of this scan was confined to 0.3 mm, since there was no signal at greater scanning distances. The reflection tomographic scans were thus performed for 7 laser positions, x_f = 0, 0.05, 0.1, 0.15, 0.2, 0.25 mm, and 13 detector positions.

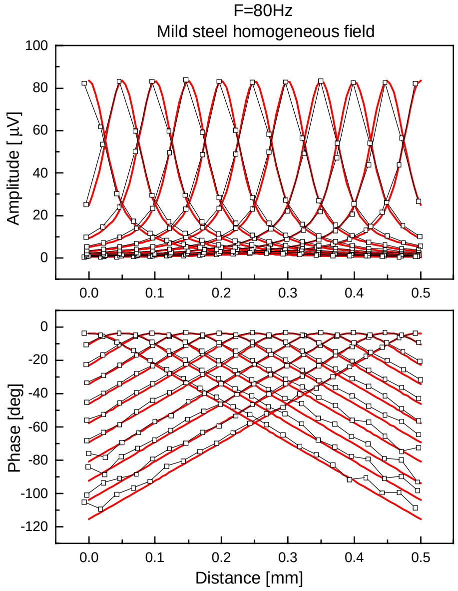

Fig. 7. Homogeneous field of sample #2 at *f=80 Hz*. Experiment (square); Theory (eq. (20a) in Ref.[6]) (solid).

5. Numerical Reconstructions

The scanned thermal wave data, for one laser position and multiple detection spots, were used as an input to reconstruct a cross-sectional slice with the method outlined in section 2. The first reconstruction performed was that of the transmission experiment, Fig. 6. Figure 8 is the average reconstruction of five laser position reconstructions obtained individually from the experimental data. In a previous work [8], it was found that averaging of reconstructions at different laser positions improves the final image, since limited information is obtained through one laser-position reconstruction. By averaging reconstructions, information from different perspectives is obtained and weighed, thus minimizing numerical artifacts. The individual numerical reconstructions were performed with laser positions at x_l = 0.5, 1.0, 1.5, 2 and 2.5 mm. The experimental amplitude and phase data of the respective laser positions were used as input parameters for the inversion technique. The frequency used in this experiment was *f=11* Hz with a thermal diffusion length of 0.56 mm. Figure 8 reconstructs the object function $F(x,y)$, with a contour of the reconstruction function at the bottom. The solid line on the contour of Figure 8 indicates the exact location and size of the defect, which was 0.6 mm in diameter, centered at (x_c=1.5 mm, y_c=1.6 mm). The defect is shown at the correct *x*-position but it extends further to the back of the sample. This is an artifact of the reconstruction, which diminishes as a wider spatial-frequency spectrum range (laser positions) is used. Furthermore, the theoretical contrast was -0.5. On averaging, information was lost because a few reconstructions underestimated the defect contrast, and only limited information was available for reconstructing the defect, since detection occurred at the back surface of the sample only. Therefore, the contrast in Fig. 8 is underestimated. In conclusion,

Received October 27, 2000; Revised December 15, 2000

the use of more laser positions for averaging reconstructions, including reflection reconstructions, would ensure better positional accuracy and contrast for the object function. The optimal regularization parameter for the reconstruction was retrieved using the L-curve method. For each reconstruction performed at a specific laser position an L-curve was plotted for selecting the optimal solution corresponding to the corner regularization parameter, σ. For one laser position the L-curve is shown in Fig. 9 and the optimal solution is $\sigma=1\times10^{-6}$. The average reconstruction was created by an average of all the optimal solutions. Figure 10 is the result of a reconstruction from the "vertical" part of the L-curve plot. The regularization parameter is $\sigma=1\times10^{-8}$. Perturbation noise dominates such a solution and the location of the defect is distorted. In Figure 11 an oversmoothed solution ("flat" part of the L-curve) is shown with the regularization parameter being σ=0.1. In this reconstruction the defect is overshadowed by the laser position x=1.5mm.

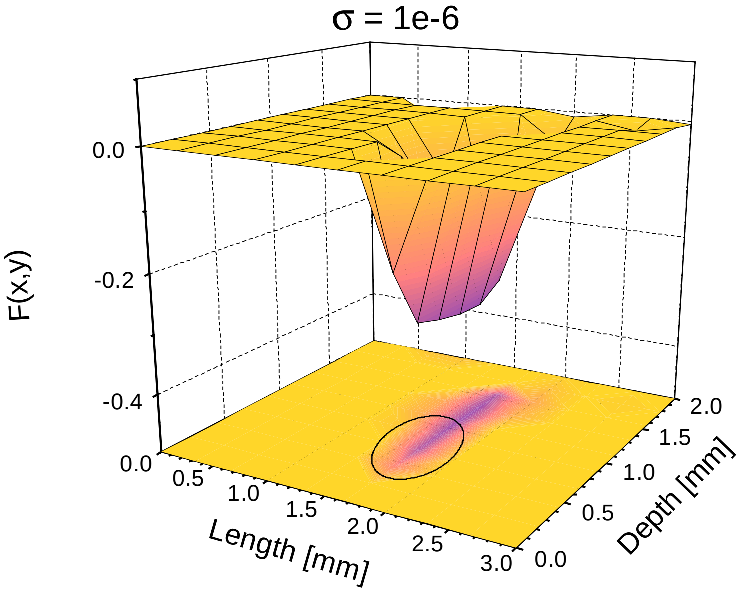

Fig. 8. TSDT transmission reconstruction of Figure 6, averaged over 5 laser positions. True defect shown by solid line; average regularization parameter $\sigma\sim1\times10^{-6}$.

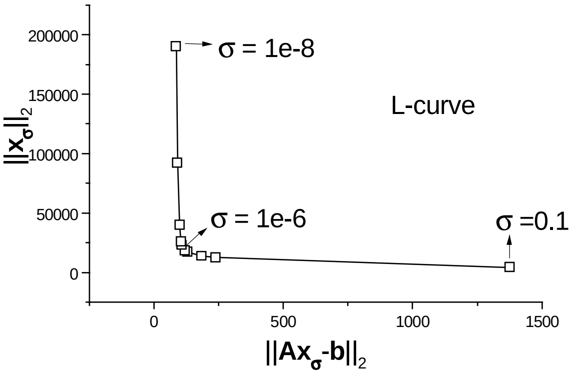

Fig. 9. L-curve of x=1.5mm laser position reconstruction of Fig. 8; optimal regularization parameter $\sigma\sim1\times10^{-6}$.

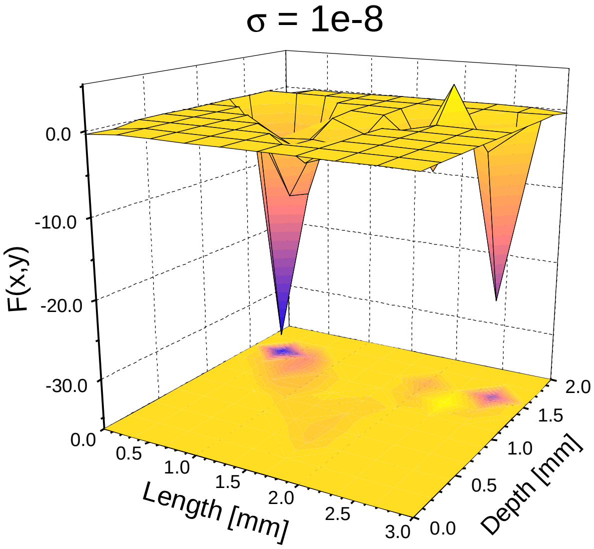

Fig. 10 Reconstruction from the vertical part of the L-curve (Fig. 9). Regularization $\sigma=1\text{x}10^{-8}$.

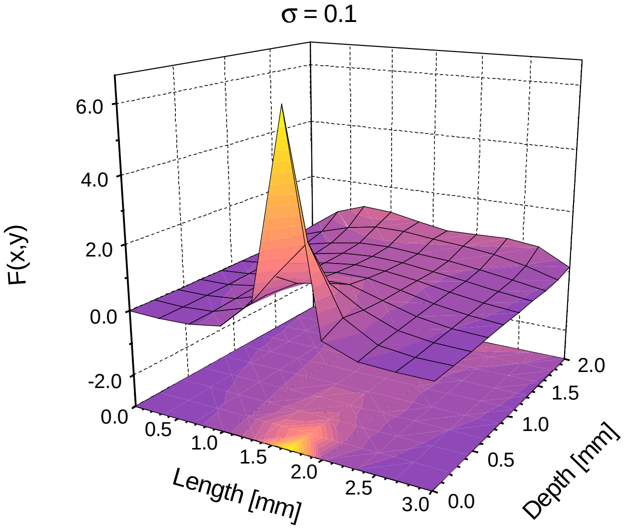

Fig. 11 Reconstruction from the flat part of the L-curve (Fig. 9). Regularization σ=0.1.

An *ill-defined* problem provides a reasonable solution after being regularized. The regularization parameter is directly proportional to the ill-conditioning of the problem. The next reconstruction was of the reflection data from a 0.1-mm-deep defect at *f=80 Hz*. Figure 12(a) is the average reconstruction of the aforementioned eleven laser positions. The optimal regularization parameter used for reconstruction was 10^{-4}. All subsequent experimental reconstructions in reflection used this regularization parameter. On the other hand, the optimal value of the regularization parameter for transmission reconstructions ($\sim 10^{-6}$) was an indication that the transmission problem was less ill-conditioned than the reflection problem. In Fig. 12 the depth position of the defect at *f=80 Hz* is correctly reproduced but the image is smaller than the true defect size shown by the solid line. Also, it is observed that the defect is somewhat asymmetric on the right hand side. This can be attributed to a slight inherent instrumental asymmetry of the photothermal radiometric microscope. The contrast is underestimated at -0.25. Some artifacts exist at the left and back surfaces of the defect. As the number of laser positions increases, these artifacts may decrease. Figure 12(b) shows the same reflection reconstruction at *f=300* Hz. Although the front of the defect is reconstructed well, the back boundary is shifted toward the front by about two thermal diffusion lengths (0.26 mm). This can be attributed to the fact that, in reflection, a scatterer can be seen no deeper than about two diffusion lengths. Deeper information is lost, resulting in severe distortions of deep-lying features. The reconstruction is, nevertheless, more symmetrical than that in Figure 12(a), as expected, since for a 0.3-mm scan the asymmetry of the instrument is much diminished.

Another reconstruction was the reflection experiment of the 0.2-mm deep defect. The modulation frequency of the experiment was 80 Hz, so that the thermal diffusion length was 0.25mm. Figure 12(c) is the average of all the reconstructions performed for each laser position. The location of the defect is in agreement with the exact position shown with the solid line. The front surface is accurately reconstructed, but the back of the defect is degraded. An instrumental asymmetry in the reconstruction is again observed on the right-hand side. Also on the back of the defect some artifacts are observed, due to the relatively small number of laser positions used. Figure 12(d) is the reflection reconstruction of the same defect for *f=300* Hz. The front surface is reconstructed well, whereas the back surface is reconstructed well up to about two thermal diffusion lengths (~ 0.25 mm) from the front surface. At the front surface some artifacts are visible. In general, most of the error related to defect location and shape in Fig. 12 is associated with the y-direction depression (loss of depth). This error occurred because the reconstruction information was obtained over a limited number of laser positions. A defect is delineated accurately on the side closer to the laser position, regardless of which mode of detection is used [8]. The experimental technique for obtaining the thermal-wave spatial-frequency spectrum is currently limited to providing information from the front or back of the sample. A tomographic scan along the perimeter of a cross-section would fill more of the spatial-frequency domain [17] and would result in a higher-fidelity reconstruction of the sample cross section.

The Born approximation seems to be adequate for the materials and defect geometries utilized in this investigation. Assuming tubular (cylindrical) defects, such as drilled holes in aluminum, Kak and Slaney [17] have given a mathematical condition for the validity of the first Born approximation for general propagating hyperbolic wave fields that obey the conventional Helmholtz wave equation. This condition can be expressed as [8,17],

$$a n_{\delta} < \frac{\lambda}{4} \tag{4}$$

where *a* is the radius of the cylindrical defect, n_δ (eq. 2b) is the *change* in the refractive index between the surrounding medium and the defect, which in this case is the square root of the ratio of background to defect thermal diffusivity**;** λ is the probe field wavelength (in the

Received October 27, 2000; Revised December 15, 2000

thermal-wave case $\lambda_{th}=2\pi\mu$). Even though there is no rigorous proof that the foregoing criterion is valid for non-propagating parabolic diffusion-wave fields [18], for all the cases examined the criterion was calculated in Table 1. It can be seen the criterion was valid for all the cases examined in this work. One issue that arises from this Table is that the criterion for reconstruction #2 is identical to that for reconstruction #4 and the criterion for reconstruction #3 is identical to #5. These cases have the same size defect located at different depths. With thermal waves the criterion of relation (4) is not strictly true, since the *depth* of the defect is as important as its *size*. In the future perhaps a better criterion can be formulated on the validity of the thermal wave Born approximation, which would include the depth of the defect.

Based on these observations, a “guide” can be formulated for optimal thermal-wave tomographic reconstructions. Reflection reconstructions can better resolve defects close to the surface. The probing frequency, and thus the thermal diffusion length, must be chosen with care. Large defects compared to the thermal diffusion length do not reconstruct as well as when the defect diameter is on the order of one thermal diffusion length. If the depth of the defect is greater than the thermal diffusion length, the defect will not be resolved depthwise. Therefore, for an optimum reconstruction the depth and size of the defect must be of the same order of one thermal diffusion length. This is consistent with the fact that in the cases examined the optimal reconstruction was that of a 0.2 mm deep defect at *f=80* Hz.

In our previous work [8] the measured experimental field was broader than the theoretical field, resulting in broadened reconstructions. A major achievement of this work is that the broadening of images has been reduced by the use of a high resolution set-up. The L-curve method of finding an optimal reconstruction proved to be an effective tool for TSDT. The only limiting factor for the reconstructions was the validity of the Born approximation in a thermal-wave field. Nevertheless, it was found that for the geometries used in this work, the Born approximation yields a large number of satisfactory results. A tomographic scan along the perimeter of a cross-section would yield more information. Reconstructing a cross-section at different frequencies may prove effective for future superposition of images and artifact rejection. A marked deterioration of images is observed as modulation frequency is increased beyond two thermal diffusion lengths as compared to the defect depth. The ability to reconstruct images is lost with increasing depth and decreasing frequency. Optimal reconstructions can be obtained in reflection when the defect depth and size are of the order of one thermal diffusion length.

Table 1. Born approximation validity for all thermal-wave reconstructions.

Reconstructions		$\alpha * n_\delta$	criterion	$\pi\mu/2=\lambda_{th}/4$
1	Transmission 0.1mm deep /F=11Hz Figure 8	0.3*0.71= **0.213mm**	<	π*0.56/2= **0.880mm**
2	Reflection 0.1mm deep / F=80Hz Figure 12(a)	0.15*0.84= **0.126mm**	<	π*0.25/2= **0.393mm**
3	Reflection 0.1mm deep /F=300Hz Figure 12(b)	0.15*0.84= **0.126mm**	<	π*0.13/2= **0.204mm**
4	Reflection 0.2mm deep / F=80Hz Figure 12(c)	0.15*0.84= **0.126mm**	<	π*0.25/2= **0.393mm**
5	Reflection 0.2mm deep /F=300Hz Figure 12(d)	0.15*0.84= **0.126mm**	<	π*0.13/2= **0.204mm**

Received October 27, 2000; Revised December 15, 2000

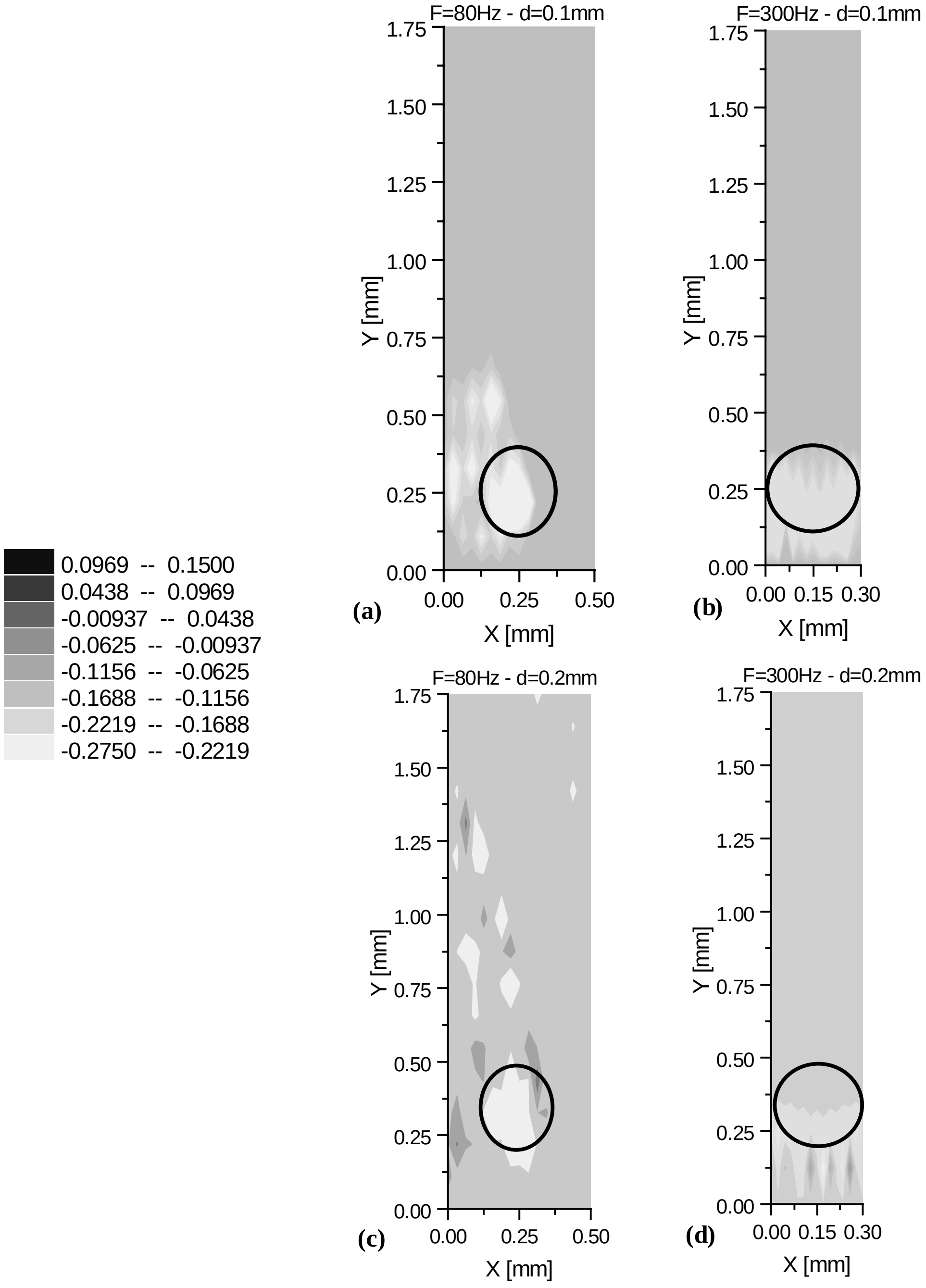

Fig. 12. Average reconstruction of 0.1-mm deep defect with 0.15-mm diameter (front is the bottom and back is the top of image): a) *f=80 Hz*, b) *f=300 Hz*. Average reconstruction of 0.2-mm deep defect with 0.15-mm diameter: c) *f=80* Hz, d) *f=300* Hz.

6. Conclusions

In this work, a robust computational method for TSDT was developed. Most importantly, the L-curve method was used to resolve the difficulty of multiplicity of solutions, thereby obtaining an optimal solution to the inverse problem. Furthermore, a new high-resolution photothermal microscope, suitable for tomographic scans and limited by the beam spot size (w=27 μm), was constructed. Machined defects were made in mild steel samples to test the performance of TSDT. It was concluded that when the defect depth and size were of the order of one thermal diffusion length, optimal reflection reconstructions were obtained.

Photothermal radiometric tomography was shown to be a method of collecting cross-sectional data, which are then numerically processed with the use of Tikhonov regularization to produce a tomogram. The implications of this work, besides establishing a reliable experimental foundation of TSDT, are quite broad in that it has the potential to address several other fields of diffusion-wave tomographic science where strong dispersive attenuation presents a reconstruction problem. These fields include medical diffuse photon-density-wave tomography, optical coherence imaging, attenuated acoustical imaging, and geophysical tomography. There are aspects that require further research in order to make TSDT a practical diffraction tomographic technique: Developments are presently being pursued to improve both the computational and experimental methodologies. There are several other methods besides Tikhonov regularization that can be investigated for solving the ill-conditioned thermal wave problem. Such methods of regularization are the truncated Singular-Value Decomposition (SVD) and the maximum-entropy, which are the subject of many publications [11]. A wavelet-based method developed by Miller *et al*. [19] appears to be very promising for data inversion and cross-sectional thermal-diffusivity tomographic imaging.

Acknowledgments

This work has been supported by the Natural Sciences and Engineering Research Council of Canada (NSERC), through a research grant.